Monodisperse Branched Molybdenum-Based Bioactive Nanoparticles Significantly Promote

Osteogenic Differentiation of Adipose-Derived Stem Cells

Wen Niu [a], Yi Guo [a, e], Yumeng Xue [a, d], Mi Chen [a], Min Wang [a], Wei Cheng [a], Bo Lei [a, b, c]∗

[a] Frontier Institute of Science and Technology, Xi'an Jiaotong University, Xi'an, China

[b]Key Laboratory of Shaanxi Province for Craniofacial Precision Medicine Research, College of Stomatology, Xi'an Jiaotong University, Xi'an 710000, China

[c] Instrument Analysis Center, Xi'an Jiaotong University, Xi'an 710054, China

[d] Department of Bioengineering, Department of Chemical and Biomolecular Engineering, Henry Samueli School of Engineering and Applied Sciences, University of California-Los Angeles, Los Angeles, CA, USA

[e] Department of Materials Science and Engineering, University of Michigan, Ann Arbor, Michigan 48109, United States

*Corresponding author

Professor Bo Lei, Xi'an Jiaotong University

Email:rayboo@xjtu.edu.cn

Abstract

Adipose-derived stem cells (ADSCs) are considered to be ideal stem cell sources for bone tissue regeneration owing to their facile obtainment and high activity. However, the regulation of osteogenic differentiation of ADSCs using biomaterials without adding growth factors is still not satisfactory. In present work, for the first time, we report molybdenum-doped bioactive glass nanoparticles with a radial porous morphology (Mo-rBGNs) and investigate their role in the osteogenic differentiation of ADSCs. The results show that Mo-rBGNs possessed the radially porous and spherical morphology, relatively homogeneous particle size (200-400 nm) and excellent apatite-forming bioactivity. Mo-rBGNs do not affect the proliferation of ADSCs, but significantly regulate their osteogenic differentiation and biominerialization. The 5% Mo-rBGNs significantly enhanced the alkaline phosphatase activity (ALP) and biominerialization ability, promoted the osteogenic genes expressions of collagen I secretion (Col I) and bone sialo protein (Bsp) in ADSCs. This study may provide a reasonable and promising strategy in designing nanoscale bioactive materials with the excellent osteogenic ability for stem cells-based bone tissue regeneration.

Keywords: Bioactive glass nanoparticles; Trace elements doping; Adipose-derived stem cells; Osteogenic differentiation;

1. Introduction

Due to the growing trauma, disease and aging of population, bone tissue defect has been a relatively common clinical disease.[1] There was increasing requirement for biomaterials to replace/repair/restore the bone tissue.[2, 3] In the field of bone tissue regeneration, stem cells-based

therapy has been recognized as a promising therapeutic option, due to their versatile differentiation capacity and bioactivity. [4, 5] As a kind of multipotent cells, mesenchymal stem cells (MSCs) retain potential of self-renewal and can differentiate into multiple kinds of cell types under suitable microenvironments. [6] As a type of mesenchymal stem cells, bone marrow MSC (BMSC) is considered to be an ideal candidate for bone tissue regeneration. [7-9] However, in recent years, more attention has been given to the promotion of osteogenesis in adipose-derived stem cells (ADSCs). [10] As compared to BMSCs, ADSCs have numerous advantages, including abundant sources, ease of isolation and a propensity to be accepted by patient. [11] The regulation of the osteogenic differentiation of ADSCs is rather essential for their clinical applications in the bone tissue regenerative medicine. [12, 13]

Various bioactive factors such as miRNA and protein/peptide have been employed to treat diseases and enhance the osteogenic differentiation of BMSCs/ADSCs. [14-17] However, the bioactive factors usually show several disadvantages including high cost and low stability. [18] Relative to conventional bioactive factors, recently bioactive materials, which can efficiently regulate the cell behavior and tissue regeneration, have been developed through their optimized design for the structure-composition. [19-22] The bioactive materials were also developed for improving the osteogenic differentiation of stem cells. [23-25] For example, bioactive silicate-based biomaterials and bioactive glasses (BGs) have shown their inherent osteogenic differentiation ability for both BMSCs and ADSCs. [26-27] BGs have become one of the best bioactive materials for bone regeneration in recent due to their biocompatibility, osteoinduced ability and controlled degradation, as well as activity. [28-34] Recent studies showed that bioactive materials with nanostructure demonstrated the enhanced capacity for enhancing soft/hard tissue regeneration *in vitro* and *in vivo*. [35-38] It was very

necessary to develop novel nanoscale bioactive materials for stimulating the osteogenic differentiation of ADSCs.

In previous studies, our group developed several monodispersed bioactive glasses nanoparticles (BGNs) for biomedical applications including bioimaging, gene/drug delivery and osteogenic differentiation of stem cells.[39-42] For example, monodispersed BGNs possessed inherent enhanced osteogenic differentiation ability for BMSCs and osteoblasts *in vitro*, as well as reinforced bone tissue regeneration *in vivo*.[43] Our previous study firstly showed that monodispersed BGNs could enhance the osteogenic differentiation of ADSCs through activating the TGF-Beta/Smad 3 signaling pathway.[44] In addition, the metallic elements such as Cu, Sr and Gd, showed their special biological functions including stimulation of osteogenesis and angiogenesis, as well as antitumor activity.[45-47] Previous study found that europium-doped BGNs (Eu-BGNs) significantly enhanced the osteogenic differentiation of human BMSCs.[48] However, europium is not the essential element of human body probably difficult to be cleared in renal, which has increased the concerns regarding the long-term toxicity. The effect of metallic elements-doped BGNs on the osteogenic differentiation of ADSCs is few reported.

By contrast, molybdenum is known to be readily absorbed from the intestinal tract and excreted mainly in the urine.[49] Molybdenum is also very important for the normal metabolism of life as a necessary trace element of organisms.[50] Furthermore, recent studies showed that molybdenum may be related to the growth of bone and tooth.[51] Therefore, it may be very promising to investigate the molybdenum doped BGNs (Mo-BGNs) as a bioactive material for regulating osteogenic of ADSCs.

In this study, we synthesize the branched monodispersed Mo-rBGNs with a radial porous structure and investigate their potential application in regulating the osteogenic differentiation of ADSCs. The physicochemical structure, biomineralization activity, cytotoxicity, as well as the effects on cellular mineralization, alkaline phosphatase activity (ALP), osteogenic protein and genes expressions of ADSCs for Mo-rBGNs, were investigated.

2. Materials and methods

2. 1 Synthesis of monodispersed Mo-rBGNs

Monodispersed Mo-rBGNs was prepared by incorporating Mo into the BGNs framework to replace role of calcium (Ca) through an ultrasonic assisted sol-gel method. Briefly, 7.5 mL was added into a solution composed of 0.15 g urea, 0.23 g isopropanol and 7.5 mL of deionized water under continuous stirring at room temperature. The mixture was allowed to react for 2 h prior to the addition of 0.675 mL TEOS. Under vigorous stirring of 30 min, the reactants were heated to 70 $^{\circ}$C were allowed to react for 7 h. Then appropriate amounts of series of reagents were added in the following sequence: TEP, $Ca(NO_3)_2 \cdot 4H_2O$, $H_8MoN_2O_4$, allowing 30 min for each reagent to react completely. After a further stirring of 16 h, the suspension was centrifuged at 10000 rpm for 15 min to collect deposits, which were further washed thrice with acetone, twice with ethanol and twice with water. Finally, these deposits were dried by a freeze-drying before calcination at 650 $^{\circ}$C for 10 h at a heating rate of 1 $^{\circ}$C min^{-1} under air conditions. The designed compositions of Mo-rBGNs were $60SiO_2:(36-x)CaO:4P_2O_5:xMo$ in mol% (x = 0, 2, 5, or 10) and designated as 0Mo-rBGNs,

2Mo-rBGNs, 5Mo-rBGNs, and 10Mo-rBGNs, accordingly. The types and sources of chemicals were shown in the supporting information.

2. 2 Physicochemical structure characterizations of Mo-rBGNs

The morphology and particle size of the Mo-rBGNs were analyzed using a transmission electron microscope (TEM, JEOL JEM-F200) working at 100 kV. The phase analysis of samples was examined by X-ray diffractometer (XRD, D/MAX-RB, Rigaku) with a Ni-filtered Cu Ka irradiation at 40 kV and 30 mA. The elemental composition of samples was determined by energy dispersive X-ray analysis (EDS, Quanta 250 FEG, FEI). The infrared spectra of the samples was obtained using a Fourier transformer infrared spectrophotometer (FT-IR, Nicolet 6700), in a wave number range of 400-4000 cm^{-1}. The analyses of surface element type and atom valance were performed using X-ray photoelectron spectroscopy (XPS, Thermo Fisher ESCALAB Xi^{+}). The surface charge of Mo-rBGNs was characterized using ζ-potential measurement on a Zetasizer Nano ZS (Nano-ZS, Malvern) instrument operating with a dynamic light scattering detector positioned at 90° and the test samples were suspended in 3 mL deionized water at a concentration of 1 mg mL^{-1}.

2.3 Biomineralization activity assessment of Mo-rBGNs

In vitro biomineralization activity was evaluated through the methodology described in our previous report where the protocol for the assessment of hydroxyapatite (HA) forming ability of bioactive glasses particles is proposed. [39] The structure and composition of formed hydroxyapatite on the surface of Mo-rBGNs was identified through XRD, FTIR and TEM respectively. The detailed procedure was shown in supporting information.

2.4 *In vitro* cellular-biocompatibility assessment of Mo-rBGNs

Adipose-derived stem cells (ADSCs, Cellbank, Shanghai) were used to investigate the *in vitro* cellular biocompatibility of Mo-rBGNs. ADSCs were obtained from ATCC (American Type Culture Collection). The cytotoxicity and cell viability of Mo-rBGNs were studied by the alamar blue assay kit (Thermo Fisher Scientific). The morphology and attachment of cells were also determined following LIVE/DEAD assay kit (Invitrogen). These testing procedures were according to the manufacturer's instructions. The supporting information showed the detailed description for cell culture, alamar blue and LIVE/DEAD analysis.

2.5 Cellular biominerialization and osteogenic differentiation analysis

The alizarin red stain (Genmed) assay was used to indicate the results of calcium deposition and extracellular-matrix mineralization of ADSCs. After incubation with differentiation medium including Mo-rBGNs in 24-well plates at a density of 2×10^4 cells/mL for 14 and 21 d, cells were fixed for 20 min using 4% paraformaldehyde, washed by PBS, stained by 200 µL alizarin for 24 h at room temperature. The stained cells were captured by a fluorescence microscope (IX53, Olympus). Finally, the calcium content of the differentiated ADSCs induced by Mo-rBGNs was calculated as the relative gray intensity of cells.

As an early marker of osteogenic differentiation, the ALP activities of ADSCs were evaluated on day 7, 14, and 21, using the SensoLyte pNPP ALP assay (AnaSpec), according to the manufacturer's instructions. The detailed procedure could be found in supporting files. The immunofluorescence staining of osteogenic proteins (COL I and BSP proteins) were assessed on 21 d. The methods and

procedures were similar with previous report with little change (Supporting information). The

quantitative real-time polymerase chain reaction (qRT-PCR) technique was employed to validate the

expression patterns of osteogenic genes including Col I and Bsp. The primers for qRT-PCR were

in Table S1. And the procedures including the extraction of total RNA and analysis of qRT-PCR were

indicated in supporting information.

2.6 Statistical analysis

The experiments were tested at least in triplicate and all data are expressed as the value mean $\pm$

standard deviation (SD) (n = 5 per group). The statistical analyses were assessed by the SPSS

software (version 13.0). The Student t test analysis of variance was employed to determine the

significant differences between different groups. $*P < 0.05$ and $**P < 0.01$ were counted statistically

significant.

3. Results and discussion

3.1 Synthesis and characterizations of Mo-rBGNs

In this work, to demonstrate the osteogenic differentiation effect of functionalized

monodispersed BGNs, Mo doped radial bioactive glass nanoparticles (Mo-rBGNs) were developed by

a modified sol-gel method (Figure 1). The osteogenic activity of Mo-rBGNs was evaluated by

detecting its effect on regulating the cellular biominerialization and expressions of osteogenic gene in

ADSCs.

The physicochemical structure characterizations of Mo-rBGNs samples are shown in Figure 2.

The as-prepared Mo-rBGNs exhibited a radially spherical morphology and a uniform diameter of

300-400 nm (Figures 2a-h, Figure S1). As shown in TEM images (Figures 2e-h), the Mo

did not produce effect on the size of Mo-BGNs, but the morphology was significantly tight upon the increase of Mo content, indicating the increase of Mo-complexes in glass network. The mean hydrodynamic diameters of 0Mo-rBGNs, 2Mo-rBGNs, 5Mo-rBGNs and 10Mo-BGNs were about 330, 320 and 423 nm with Zeta potentials of -10.4, -7.26, - 7.13 and -4.89 mV, respectively (Figure The morphology and element composition of Mo-rBGNs were also analyzed by high resolution SEM (Figures 2j-k). The energy dispersive spectra (EDS) mapping of 10Mo-rBGNs showed that Si and Mo were evenly distributed within the whole nanoparticles (Figure S2). The EDS analysis confirmed that the detected Mo/Si molar ratio resulted in fair agreement with the theoretical ratio (Figures 2l-o). Additionally, as the increase of the intensity of Mo peak, the calcium decreased because Ca was substituted by Mo complexes in the glass compositions. Such findings indicate that Mo was incorporated in the silicate structure of the glasses.

The phase structure and chemical structure of xMo-BGNs were further analyzed by XRD, FTIR and XPS (Figure 3). In the XRD patterns of Mo-rBGNs (Figure 3a), the broad peak at 23° was corresponded to amorphous silica, and the diffraction peaks at $2\theta = 18.6, 28.8, 31.2, 34.3, 47.1, 49.3$ 58.0° were attributed to (101), (112), (004), (200), (204), (220) and (312) reflections of $CaMoO_4$ (JCPDS 29-0351). The above analyses suggest that the phase structure of Mo-rBGNs was affected by the addition of Mo. As shown in FTIR (Figure 3b), the bands located at around 860 cm^{-1}, 898 cm^{-1}, 1000 cm^{-1} were assigned to the bending vibration of Si-O-Si, the asymmetrical stretching mode of Mo-O-Mo and the symmetrical stretching mode Si-O-Si, respectively. Moreover, the of a band at around 1631 cm^{-1} was caused by the -OH groups in water molecules. The characteristic bands of Si–O–Si were significantly weakened upon the increase of Mo content, indicating the

of glass network integrity and the appearance of molybdenum phase. The XPS analysis showed that surface of 10Mo-BGNs was composed of Ca, O, Si and Mo elements (Figure 3c) and the typical XPS two-peak shaped of Mo 3d spectrum could be observed (Figure 3d). This pair of strong peaks located 231.2 and 234.5 eV could be attributed to the Mo^{6+}. These results demonstrated that monodispersed Mo-rBGNs with uniform size was synthesized successfully by the ultrasonic assisted template technique.

3.2 Biomineralization activity analysis of Mo-rBGNs

In order to explain the bone-bonding ability and osteogenic bioactivity of Mo-rBGNs, the were soaked into SBF for various times to evaluate the biological apatite-forming ability (biomineralization activity). After immersion in SBF for 1 d, the structure and morphology of Mo-rBGNs were no significantly changed (Figure 4a-c, Figure S3). After further soaking in SBF, the XRD diffraction patterns (Figure 4d) of Mo-rBGNs demonstrated peaks at approximately 31.7, 36.4, 45.4 and 56.6° which corresponded to the lattice planes (112), (202), (222) and (211) of (JCPDS 09-0432). And two characteristic peaks at 596 and 604 cm^{-1} corresponding to the P-O bands PO_4^{3-} of crystalline Ca-P were seen in the FTIR spectra (Figure 4e) after soaking for 3 d. These new peaks of FTIR spectra and XRD patterns became significantly stronger upon the increase of the time (Figures 4g, 4h). Additionally, after soaking Mo-rBGNs in SBF for 3 and 7 d, TEM that the deposited apatite layer possessed a flake-like morphology which was the typical morphology hydroxyapatite (Figures 4f, 4i, Figure S4, Figure S5). In summary, the above results confirmed the apatite-forming ability of Mo-rBGNs implying their possible bone-bonding capability *in vivo* and Mo incorporation did not affect the excellent biomineralization of BGNs.

3.3 Cellular biocompatibility evaluation

ADSCs were employed as the model to analyze the cellular biocompatibility of Mo-rBGNs.
After incubation with samples (40-200 μg mL^{-1}), ADSCs exhibited good cell attachment morphology
(Figure 5a, Figure S6). Specifically, as shown in Figure 5a, after treatment with nanoparticles at 80 μg
mL^{-1} for 72 h, significantly higher numbers of living cells (green fluorescence) were observed as
compared with Blank, demonstrating that samples at this safe concentration could support cell growth.
However, at the high particle concentration (120 and 200 μg mL^{-1}), poor attachment morphology was
observed between different Mo-rBGNs groups and Blank. These results indicated that the suitable
concentration of Mo-rBGNs could improve cell proliferation. In addition, at day 1, Mo-rBGNs with
40 μg mL^{-1} demonstrated significantly higher cell viability compared to that of Blank. The cell
viability showed a significant decrease upon the increase of concentration (Figure 5b). Notably, the
relative cell viability values of 5Mo-rBGNs showed that the cells could efficiently proliferate after
culture for 72 h with nanoparticles at a concentration of 40 to 80 μg mL^{-1} (Figure 5c). Our results
demonstrated that Mo-rBGNs with specific Mo content at a safe concentration could efficiently
enhance cellular biocompatibility which may be a great benefit to their application of osteogenic
differentiation.

3.4 Osteogenic differentiation analysis

The ALP activity and mineralized nodule formation are an early stage marker for osteogenic
differentiation and a phenotypic marker for mature osteoblasts. The ALP activities measured in
following incubation with Mo-rBGNs (30-90 μg mL^{-1}) under osteoinductive conditions were detected
at day 7 and 14. Figures 6a, 6b show that the relative ALP activities in all samples were significantly

increased with culture times. On day 7, for 2Mo-rBGNs and 5Mo-rBGNs, the ALP activities were significantly increased with increasing particle concentration, with no significant differences observed between other groups. After incubation with Mo-rBGNs from 30-90 μg mL^{-1} for 14 d, the ALP activities were all higher than Blank. These results showed that low-content Mo (2 and 5 mol %) rBGNs with suitable concentration could effectively enhance the ALP activity of ADSCs. The deposition and mineralization of Mo-rBGNs were detected by alizarin red stain and relative intensity calcium-content examination (Figures 6c, 6d). Compared with blank, Mo-rBGNs groups with concentration of 60 μg mL^{-1} demonstrated significantly stronger alizarin red staining after a 21 d incubation, suggesting positive calcium mineralization (Figure 6c). The relative gray intensity of calcium-content detection in ADSCs was performed following treatment with different concentrations of materials for 21 d (Figure 6d). We observed that the relative gray intensity of calcium content was significantly enhanced by incubation with 5Mo-rBGNs of 60 μg mL^{-1} relative to the blank; however, there were no significant difference in calcium content between the different concentration groups on day 21 (Figure 6d, Figure S2). The results from alizarin red staining and relative gray intensity of calcium-content analysis suggested that the optimized Mo-doped rBGNs significantly improved mineralization capability of ADSCs.

To demonstrate the effect of Mo-rBGNs at the concentration of 60 μg mL^{-1} on the osteogenic differentiation of ADSCs at the mRNA level, we determined the expressions of early-stage osteoblastic marker genes (Col I) and late-stage marker (Bsp) in cells after culture for various periods (Figure 7). The Col I expression on day 7 was firstly upregulated after incubation with Mo-BGNs at a low-content Mo-doped and followed by the decreased at 5Mo-rBGNs (Figure 7a). On day 14, no

significant difference of Col I expression among various groups was observed (Figure 7b). For Bsp

expression, on day 7 and 14, 2Mo-rBGNs group with 60 μg mL^{-1} showed the significantly high Bsp

level, as compared with blank and other groups (Figures 7c, 7d, Figure S7). These results suggested

that the Mo-rBGNs could dramatically enhance the osteogenic genes expression in ADSCs.

Additionally, the immunofluorescence staining for COL I and BSP proteins on day 21 were

investigated to demonstrate the continuity effect of Mo-rBGNs on ADSCs osteogenic proteins

expression. COL I and BSP were shown respectively as green and red while nuclei were stained as

blue. Both of early and late stage proteins in blank groups expressed no obvious positive COL I and

BSP staining (Figure 8a). However, the significant fluorescence intensity associated with COL I

expression continued to increase from 0 to 5 mol % of Mo doped rBGNs, reaching peak values at 5

mol% (Figure 8b). Under the same osteoinductive condition, the BSP protein expression showed a

similar tendency with the positive COL I protein staining and 5Mo-rBGNs showed observably higher

fluorescence intensity associated with BSP expression comparing with other groups (Figure 8c). The

ALP activity, Alizarin Red staining, osteogenic genes analysis and immunofluorescence staining

further demonstrated that Mo-rBGNs could efficiently enhance the osteogenic differentiation of

ADSCs.

4. Conclusion

In summary, monodispersed Mo-rBGNs were fabricated by an ultrasonic assisted template method.

Mo-rBGNs showed a uniform spherical porous morphology with a particle size of 300-400 nm. The

Mo-rBGNs could efficiently induce the formation of biological apatite layer under SBF environment,

indicating their excellent biomineralization activity. Our Mo-rBGNs significantly enhanced the

osteogenic differentiation of ADSCs through improving their ALP activity, calcium mineralization,

osteogenic proteins, and genes expressions. This study firstly suggests that the rBGNs with low

content Mo doping could effectively enhance the biominerialization and osteogenic differentiation of

ADSCs, suggesting their great potential for ADSCs-based bone tissue regeneration.

Acknowledgements

References

1   H. Petite, U. Viateau, W. Bensaïd, A. Meunier, C. Pollak, M. Bourguignon, K. Oudina, L. Sedel,

Guillemin, *Nat. Biotechnol.*, 2000, **18**, 956-963.

2   C. Yang, X. Wang, B. Ma, H. Zhu, Z. Huan, N. Ma, C. Wu, J. Chang, *ACS Appl. Mater. Interfaces*, 2017,

9, 5757-5767.

3   F. Zhao, B. Lei, X. Li, Y. Mao, R. Wang, D. Chen, X. Chen, *Biomaterials*, 2018, **178**, 36-47.

4   B. Sui, C. Hu, A. Liu, C. Zheng, K. Xuan, Y. Jin, *Biomaterials*, 2017, **10**, 046.

5   M. Wang, Y. Guo, M. Yu, P. X. Ma, C. Mao, B. Lei, *Acta Biomater.*, 2017, **54**, 69-80.

6   M. Gnecchi, P. Danieli, G. Malpasso, M. C. Ciuffreda, *Methods Mol. Biol.*, 2016, **1416**, 123-146.

7   T. L. Tsai, W. Li, *Stem Cell Rep.*, 2017, **8**, 387-400.

8   E. E. L. Lewis, H. Wheadon, N. Lewis, J. Yang, M. Mulling, A. Hursthouse, D. Stirling, M. J. Dalby, C. C. Berry, *ACS Nano*, 2016, **10**, 8346-8454.

9   Y. Wang, X. Chen, W. Cao, Y. Shi, *Nat. Immunol.*, 2014, **15**, 1009-1016.

10   W. Li, Y. Liu, P. Zhang, Y. Tang, M. Zhou, W. Jiang, X. Zhang, G. Wu, Y. Zhou, *ACS Appl. Mater. Interfaces*, 2018, **10**, 5240-5254.

11   R. Dai, Z. Wang, R. Samanipour, K. I. Koo, K. Kim, *Stem Cells Int.*, 2016, **2016**, 6737345.

12   S. Zhang, B. Ma, F. Liu, J. Duan, S. Wang, J. Qiu, D. Li, Y. Sang, C. Liu, D. Liu, H. Liu, *Nano Lett.*, 2018, **18**, 2243-2253.

13   C. Fan, L. Jia, Y. Zheng, C. Jin, Y. Liu, H. Liu, Y. Zhou, *Stem Cell Rep.*, 2016, **7**, 236-248.

14   X. Qu, Z. Liu, B. Ma, N. Li, H. Zhao, T. Yang, Y. Xue, X. Zhang, Y. Shao, Y. Chang, J. Xun, B. Lei, Y. Du, *Nano Res.*, 2019, **12**, 593-599.

15   Q. Huang, Y. Zou, M. C. Arno, S. Chen, T. Wang, J. Gao, A. P. Dove, J. Du, *Chem. Soc. Rev.*, 2017, **46**, 6255-6275.

16   M. K. Nguyen, O. Jeon, M. D. Krebs, D. Schapira, E. Alsberg, *Biomaterials*, 2014, **35**, 6278-6286.

17   R. A. Marklein, J. A. Burdick, 2010, **22**, 175-189.

18   E. R.Balmayor, J. P. Geiger, M. K. Aneja, T. Berezhanskyy, M. Utzinger, O. Mykhaylyk, C. Rudolph, C. Plank, *Biomaterials*, 2016, **87**, 131-146.

19 Y. Li, N. Li, J. Ge, Y. Xue, W. Niu, M. Chen, Y. Du, P. X. Ma, B. Lei, *Biomaterials*, 2019, **201**, 68-76.

20 M. Wang, Y. Guo, Y. Xue, W. Niu, M. Chen, P. X. Ma, B. Lei, *Biomaterials*, 2019, **199**, 10-21.

21 C. Wang, M. Wang, T. Xu, X. Zhang, C. Lin, W. Gao, H. Xu, B. Lei, C. Mao, *Theranostics*, 2019, **9**, 65-76.

22. L. Zhou, Y. Xi, Y. Xue, M. Wang, Y. Liu, Y. Guo, B. Lei, *Adv. Funct. Mater.*, 2019, doi.org/10.1002/adfm.201806883.

23 O. Chaudhuri, L. Gu, D. Klumpers, M. Darnell, S. A. Bencherif, J. C. Weaver, N. Huebsch, H. Lee, E. Lippens, G. N. Duda, D. J. Mooney, *Nat. Mater.*, 2016, **15**, 326-332.

24 M.Bohner, G. Baroud, A. Bernstein, N. Dobelin, L. Galea, B. Hesse, R. Heuberger, S. Meille, P. Michel, B. V. Rechenberg, J. Sague, H. Seeherman, *Mater. Today*, 2017, **20**, 106-115.

25 T. Ting, W. Xie, W. Gao, G. Wang, L. Zeng, G. Miao, B. Lei, Z. Lin, X. Chen, *Front.Chem.,* 2019, **7**, 186.

26 B. Lei, K. H. Shin, Y. H. Koh, H. E. Kim, *J. Biomed. Mater. Res. A*, 2014, **102**, 1528-1536.

27 J. Hum, A. R. Boccaccini, *Int. J. Mol. Sci.,* 2018, **19**, 1807.

28 B. Lei, X. Chen, Y. Wang, N. Zhao, C. Du, L. Fang, *Biomed. Mater.*, 2010, **5**, 054103.

29 Y. Zhou, M. Shi, J. R. Jones, Z. Chen, J. Chang, C. Wu, Y. Xiao, *Int. Mater. Rev.*, 2017, **62**, 392-414.

30 Y. Xue, Z. Zhang, W. Niu, M. Chen, M. Wang, Y. Guo, C. Mao, C. Lin, B. Lei, *Part. Part. Syst. Charatc.*, 2019, 1800507.

31 L. L. Hench, J. M. Polak, *Science*, 2002, **295**, 1014-1017.

32 B. Lei, X. Chen, X. Han, J. Zhou, *J. Mater. Chem.*, 2012, **22**, 16906-16913.

33 A. El-Fiqi, T. H. Kim, M. Kim, M. Eltohamy, J. E. Won, E. J. Lee, H. W. Kim, *Nanoscale*, 2012, **4**, 7475-7488.

34 W. Gao, W. Jin, Y. Li, L. Wan, C. Wang, C. Lin, X. Chen, B. Lei, C. Mao, *J. Mater. Chem. B.*, 2017, **5**, 7285-7296.

35 J. Ge, K. Liu, W. Niu, M. Chen, M. Wang, Y. Xue, C. Gao, P. X. Ma, B. Lei, *Biomaterials*, 2018, **175**, 19-29.

36 Y. Xi, J. Ge, Y. Guo, B. Lei, P. X. Ma, *ACS Nano*, 2018, **12**, 10772-10784.

37 A. Bachhuka, B. Delalat, S. R. Ghaemi, S. Gronthos, N. H. Voelcker, K. Vasilev, *Nanoscale*, 2017, **9**, 14248-14258.

38 B. Holmes, K. Bulusu, M. Plesniak, G. L. Zhang, *Nanotechnology*, 2016, **27**, 064001.

39 Y. Xue, Y. Du, J. Yan, Z. Liu, P. X. Ma, X. Chen, B. Lei, *J. Mater. Chem. B*, 2015, **3**, 3831-3839.

40 M.Yu, Y. Xue, P. X. Ma, C. Mao, B. Lei, *ACS Appl. Mater. Interfaces*, 2017, **9**, 8460-8470.

41 Y. Xue, Y. Guo, M. Yu, M. Wang, P. X. Ma, B. Lei, *Adv. Healthcare Mater.*, 2017, **6**, 1700630.

42 Y. Li, Y. Guo, W.Niu, M. Chen, Y. Xue, J. Ge, P. X. Ma, B. Lei, *ACS Appl. Mater. Interfaces*, 2018, **10**, 17722-17731.

43   M. Yu, B. Lei, C. Gao, J. Yan, P. X. Ma, *Nano Res*., 2017, **10**, 49-63.

44   Y. Guo, Y. Xue, W. Niu, M. Chen, M. Wang, P. X. Ma, B. Lei, *Part. Part. Syst. Charatc*., 2018, **35**, 1800087.

45   A.Bari, N. Bloise, S. Fiorilli, G. Novajra, M. Vallet-Regi, G. Bruni, A. Torres-Pardo, J. M. Gonzalez-Calbet, L. Visai, C. Vitale-Brovarone, *Acta Biomater*., 2017, **55**, 493-504.

46   D. Bellucci, V. Cannillo, *Mater. Lett*., 2018, **213**, 67-70.

47   M. Wu, Y. Xue, N. Li, H. Zhao, B. Lei, M. Wang, J. Wang, M. Luo, C. Zhang, Y Du, C. Yan, *Angew. Chem. Int. Ed*., 2019, doi.org/10.1002/ange.201812972.

48   F. Li, M. Wang, G. Pi, B. Lei, *J. Biomed. Nanotechnol*., 2018, **14**, 756-764.

49   E. C. Derenzo, E. Kaleita, P. G. Heytler, J. J. Oleson, B. L. Hutchings, J. H. Williams, *Arch. Biochem. Biophys.*, 1953, **45**, 247-253.

50   I. A. Castro, R. S. Datta, J. Ou, A. Castellanos-Gomez, S. Sriram, T. Daeneke, K. Kalantar-Zadeh, *Adv. Mater*., 2017, **29**, 1701619.

51   K. Nganvongpanit, K. Buddhachat, P. Piboon, T. Euppayo, P. Mahakkanukrauh, *Forensic Sci. Int*., 2017, **271**, 33-42.

TOC and summary
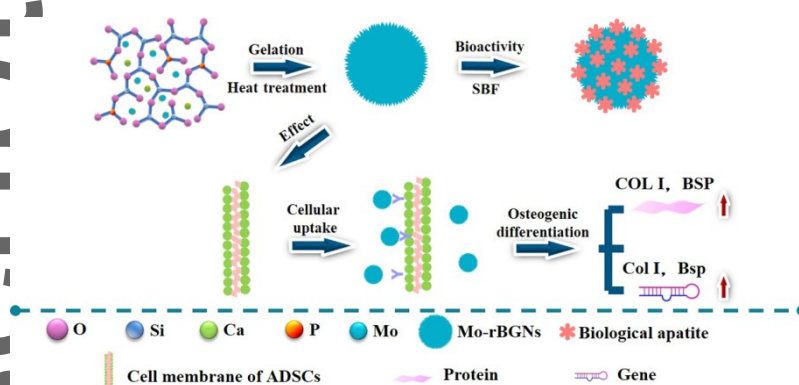
Summary

We report molybdenum-doped bioactive glass nanoparticles with a radial porous morphology (Mo-rBGNs). Mo-rBGNs possessed excellent apatite-forming bioactivity, significantly regulate the osteogenic differentiation and biominerialization of adipose-derived stem cells (ADSCs). The 5% Mo-rBGNs significantly enhanced the alkaline phosphatase activity (ALP) and osteogenic genes expressions of collagen I secretion (Col I) and bone sialo protein (Bsp) in ADSCs.
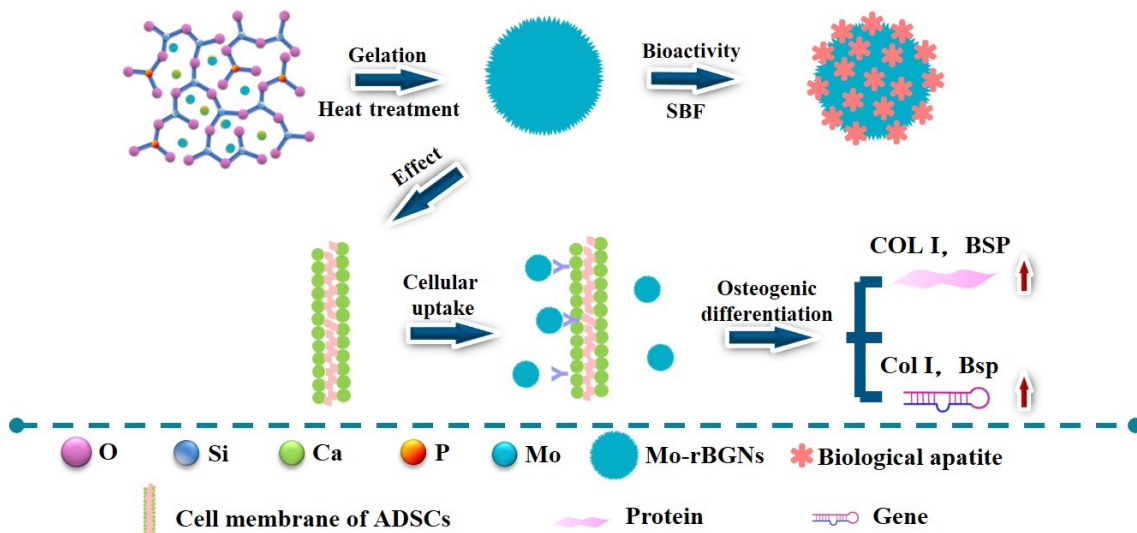
Figure 1 Schematic illustration describing the synthetic route of Mo-rBGNs and their potential biomedical applications *in vitro* and *in vivo*.
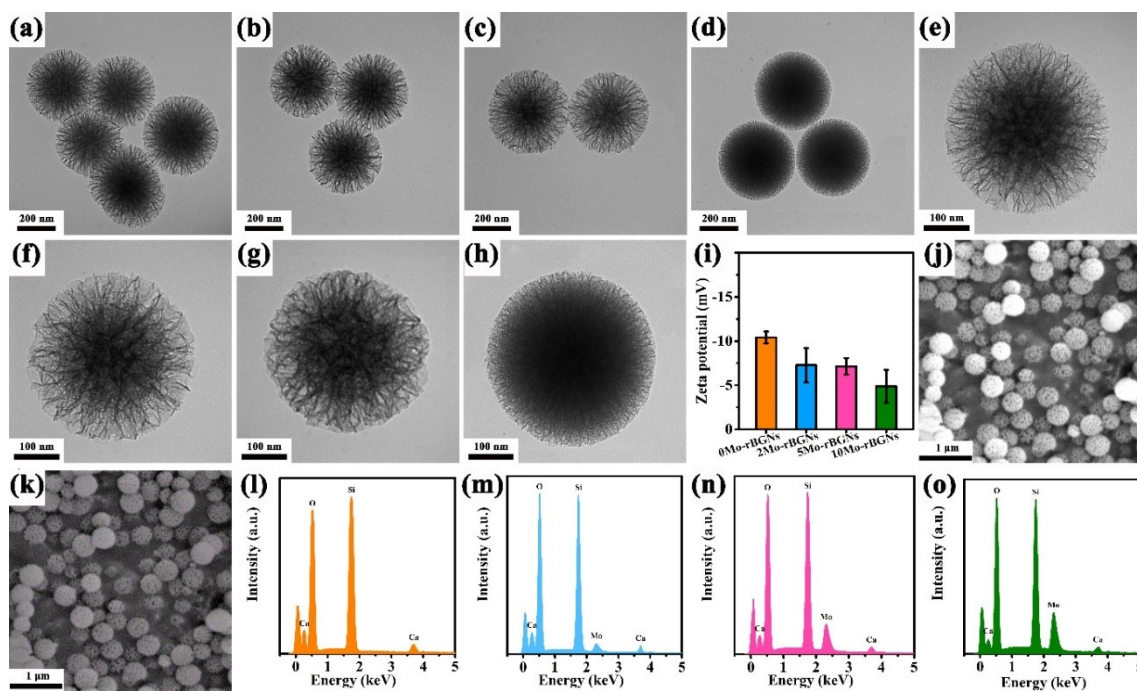
Figure 2 Morphology evaluation of Mo-rBGNs. (a-d) TEM images of 0Mo-rBGNs (a), 2Mo-rBGNs (b), 5Mo-rBGNs (c) and 10Mo-rBGNs (d) (scale bar: 200 nm); (e-h) High magnification TEM pictures (scale bar: 100 nm); (i) Zeta-potential analysis (*p < 0.05; **p < 0.01); (j)SEM image of 10Mo-rBGNs (scale bar: 1 μm); (k) EDS mapping of 10Mo-rBGNs (scale bar: 1 μm); (l-o) EDS spectra of 0Mo-rBGNs, 2Mo-rBGNs, 5Mo-rBGNs and 10Mo-rBGNs.
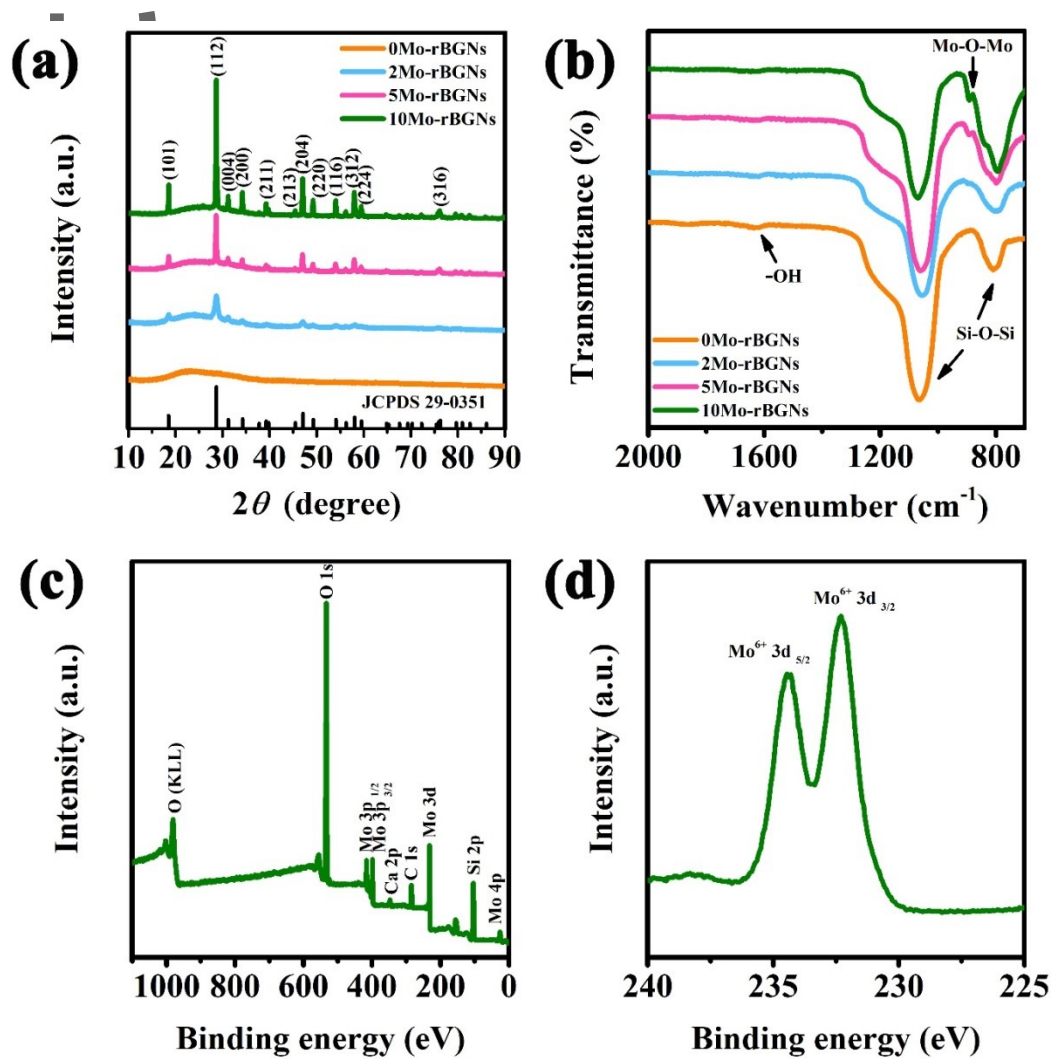
Figure 3 Characterizations of Mo-rBGNs. (a,b) XRD patterns (a) and FTIR spectra (b) of

Mo-rBGNs; (c) XPS spectrum of 10Mo-rBGNs; (d) Mo 3d peaks in XPS spectra of 10Mo-rBGNs.
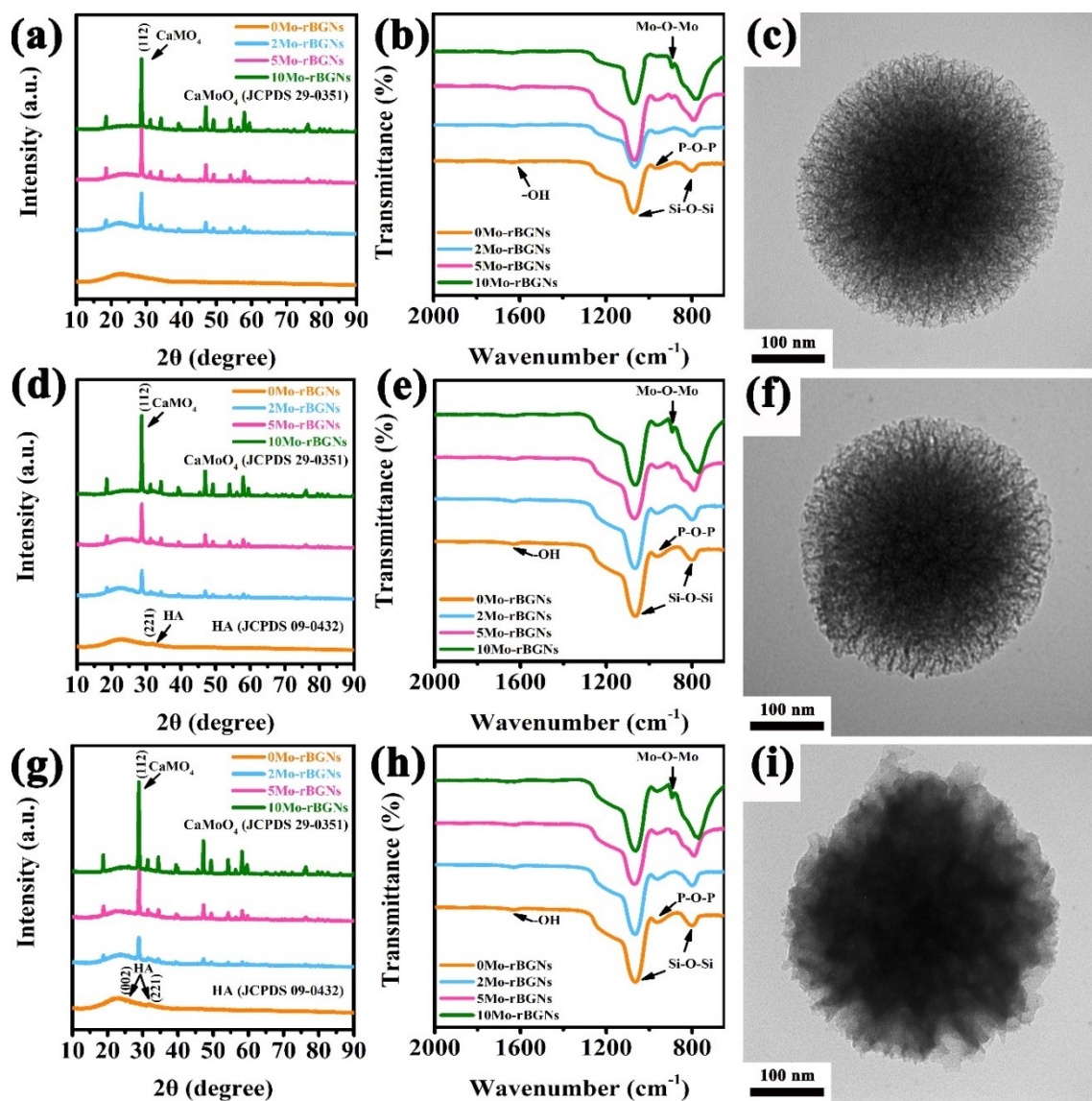
Figure 4 Biomineralization activity evaluation of Mo-rBGNs. (a-c) XRD patterns (a), FTIR spectra (b) of Mo-rBGNs and TEM image (c) of 10Mo-rBGNs after biomineralization for 1 d (scale bar: 100 nm); (d-f) XRD patterns (d), FTIR spectra (e) of Mo-rBGNs and TEM image (f) of 10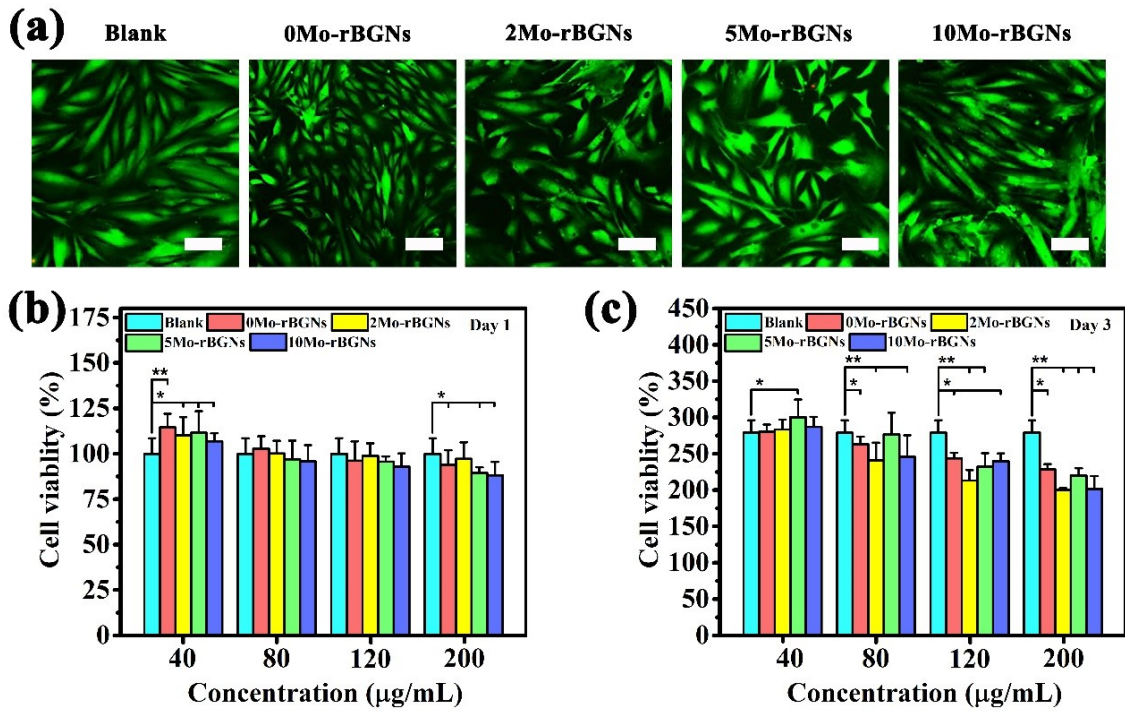Mo-rBGNs after biomineralization for 3 d (scale bar: 100 nm); (g-i) XRD patterns (g), FTIR spectra (h) of Mo-rBGNs and TEM image (i) of 10Mo-rBGNs after biomineralization for 7 d (scale bar: 100 nm).

Figure 5 Cellular biocompatibility evaluation of ADSCs following incubation with various concentrations of Mo-rBGNs. (a) Fluorescence images indicating live-dead staining after a 3 d incubation (scale bar: 100 µm); (b, c) Cell viability and proliferation after culture for 1 (b) to 3 d (c) (*$p < 0.05$; **$p < 0.01$). The solution without nanoparticle was used as the negative control (Blank).
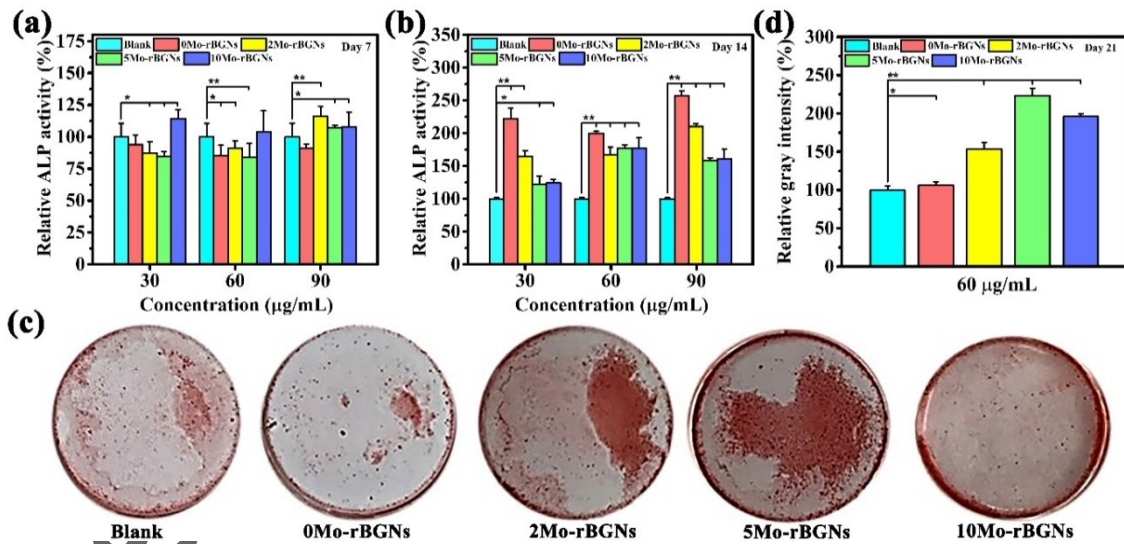
Figure 6 *In vitro* ALP activity evaluation and calcium deposition biomineralization staining evaluation of ADSCs following induction by Mo-rBGNs. (a, b) ALP activity on day 7 (a) and 14 (b) (*$p < 0.05$; **$p < 0.01$); (c) The relative gray intensity based on the images of Alizarin red staining; (d) Alizarin red staining of ADSCs (*$p < 0.05$; **$p < 0.01$).
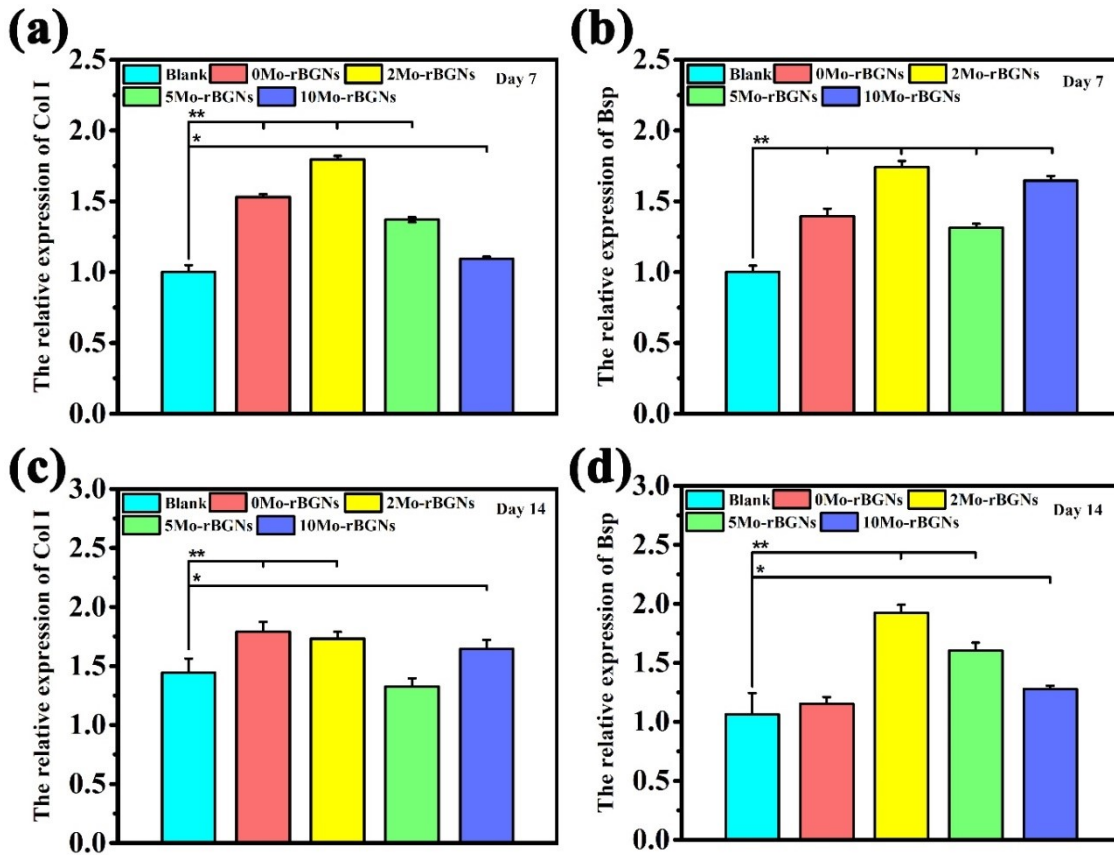
Figure 7 Relative expression of osteoblastic marker gene during osteogenic differentiation following induction by Mo-rBGNs with 60 μg mL^{-1} on day 7 and 14. (a, b) Relative expression of Col I (a) and Bsp (b) on day 7; (c, d) Relative expression of Col I (c) and Bsp (d) on day 14. *$p <$ 0.05; **$p <$ 0.01.
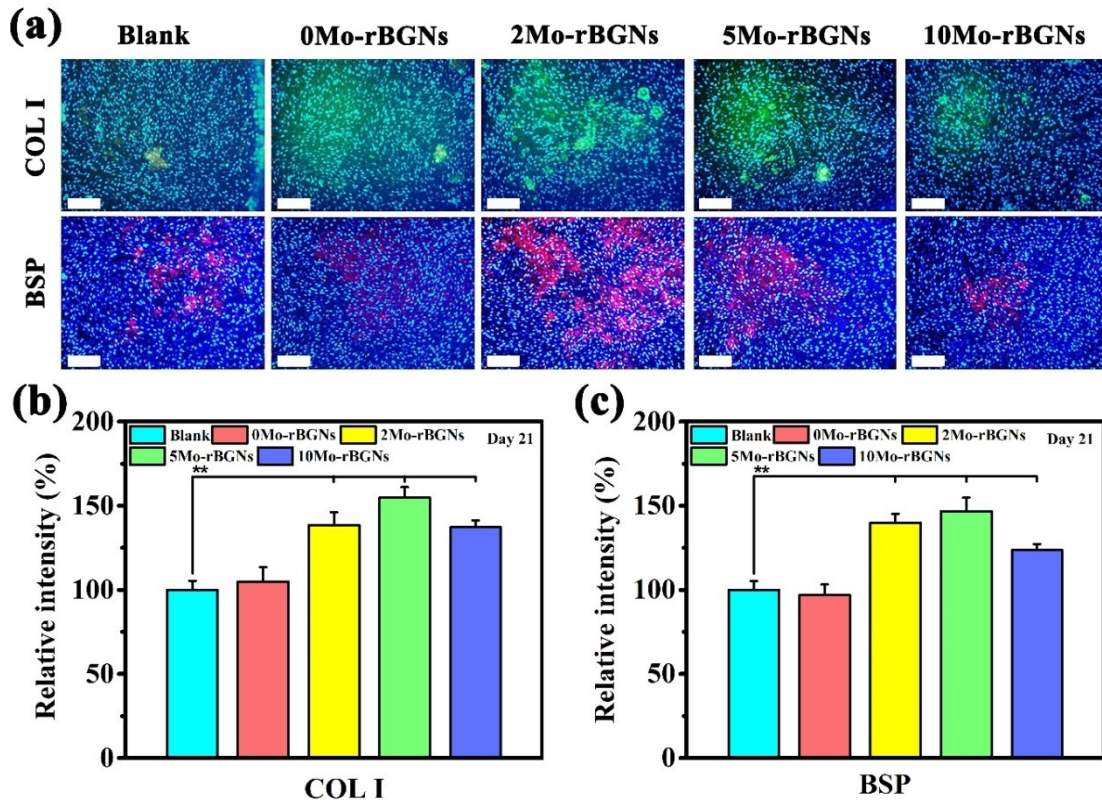
Figure 8 Immunofluorescence staining for the COL I and BSP proteins in ADSCs on day 21 after incubated with 60 μg mL^{-1} Mo-rBGNs. (a) Immunofluorescent staining of COL I and BSP proteins (scale bar: 100 μm); (b) Relative fluorescent intensity of COL I protein (*$p < 0.05$; **$p < 0.01$); (c) Relative fluorescent intensity of BSP protein (*$p < 0.05$; **$p < 0.01$).